Determination of Vertical Profiles of Shell Currents in the Ionosphere

Evgeny Romashets[1] and Marek Vandas[2]

[1]Department of Physics, Lamar University Beaumont, Texas, USA
[2]Astronomical Institute of the Czech Academy of Sciences, Prague, Czech Republic

Correspondence: Evgeny Romashets (eromashets@lamar.edu)

Abstract. In previous works, we found Euler potentials for the combined magnetic field of Earth's dipole, field aligned currents, ring current, and the magnetopause surface currents (represented by Dungey's term), in the magnetosphere. Field aligned currents, also known as the Birkeland currents, experience closure in the ionosphere, through the shell-current patterns, also known as the Pedersen and Cowley currents. Field aligned currents can be measured at an altitude of 800 km, farther, or closer, and can be reconstructed in the entire magnetosphere with tracing along the magnetic field lines. The determination of shell currents is more difficult. They can only be measured in the ionosphere, because they form a closure of field aligned currents in the ionosphere. Analytical and numerical modelings of the shell currents are not easy tasks and require knowledge of the conductivity tensor in the ionosphere. We propose an alternative approach for the shell currents modeling. In this paper, we determine current density distribution in a finite thickness ionosphere. Our system consists of the ionosphere, a region above it (outer region) and a region below it (inner region). The dipole field is present in the entire system. In addition, there is a field generated by the field aligned currents in the outer region. We search for a continuation of these currents into the ionosphere, for shell currents.

1 Introduction

Kintner et al. (1974) deduced shell and field-aligned currents (FACs) during the March 16, 1973 substorm. They reported a southward current density of 14.37 μA m^{-2}, a westward current density of 22.5 μA m^{-2}, and a FAC density of 5 μA m^{-2}. The latter current was concentrated at heights of 120–190 km. A southward electric field of 60 mV m^{-1} identified southward currents as shell (Pedersen) currents. Westward (Cowley) currents were considered as Hall currents, flowing perpendicularly to the electric field due to the Hall conductivity in the ionosphere. Rostoker and Hron (1975) explained eastward and westward electrojets in the ionosphere, as well as their interrelations with convection in the magnetosphere. The electrojets are caused by precipitation of high energy electrons ($E > 20$ keV). Kamide and Brekke (1977) determined altitudes of the auroral electrojets in the ionosphere during disturbed periods. It was found that the eastward electrojet is located at 120 km and the westward electrojet at 100 km. Banks and Yasuhara (1978) studied the electric field of the night time ionospheric E-region. They found that relatively large electric fields can exist in the absence of shell currents in the ionosphere, because of insufficient particle precipitation. Troshichev et al. (1979) noticed that the shell currents effect can be significant on Earth's surface and it is not

canceled by distant FACs during moderate and strong geomagnetic storms. Opgenoorth et al. (1983) determined the structure of the electric currents system in the vicinity of a westward traveling surge. A counterclock loop of currents around a leading edge of the surge was revealed. Senior et al. (1982) noticed that the westward electrojet in the ionosphere extends across the Region 2 / Region 1 boundary in the ionosphere morning sector and that the Region 2 FACs are closed by southward

30 Pedersen currents within the ionosphere. Raghavarao et al. (1984) found that the ionization density at 100 km increases by a factor of 2 to 10 from the time of sunset to midnight and the plasma density centered around 120 km altitude deepens by a factor of 2 to 5 during the same period. Baumjohann (1982) reviewed studies of field-aligned and shell currents. Araki et al. (1989) investigated the geomagnetic effects of the Hall and Pedersen currents flowing in the auroral ionosphere. They found that in July 1987, the northward currents contribution to the H-component was 0.56 nT, while that of eastward currents

35 was in the range 0.14–0.20 nT. Kirkwood et al. (1988) determined that the highest observed conductance for northward ionospheric currents was 48 S, and for eastward currents 120 S. Werner and Ferraro (1990) showed that the vertical profiles of the shell current density in the E and D layers can be obtained with a high-power auroral stimulation (HIPAS) heating facility. The behavior of these ionospheric currents can be deduced from a comprehensive study of extremely low frequency (ELF) signals received at a local field site. Devasia and Reddy (1995) presented a method to retrieve the height-varying

40 east-west wind in the equatorial electrojet from the local wind-generated electric field, or from the radar-measured phase velocity of the type II plasma waves. Galand and Richmond (2001) proposed a simple parameterization for the Pedersen and Hall conductances produced by proton precipitation. Their derivation is based on a proton transport code for computing the electron production rate and on an effective recombination coefficient for deducing the electron density. Amm (2001) utilized Cluster II mission data which provides the possibility to instantaneously obtain spatially distributed measurements

45 of FACs from a fleet of satellites; and presented the "elementary current method" that combines such measurements mapped to the ionosphere with two-dimensional ground magnetic data, to calculate actual ionospheric currents, without the need for further assumptions. Hosokawa et al. (2010) presented an appearance of the shell current layer carried by the electrons in the auroral D-region. Such a layer was detected by the EISCAT VHF radar in Tromsø, Norway when an intense pulsating aurora (PA) occurred. Amm and Fuji (2008) commented on a long-standing debate on to what extent the strong upward FACs in a

50 substorm breakup spiral are either closed by downward FAC through Pedersen currents flowing radially to the center of the spiral (local closure) or by currents that flow westward though a Cowling channel which extends in the region eastward of the spiral (Cowling closure). They showed that for the pseudobreakup spiral event on February 3, 1999, 68 percent of the upward FAC in the spiral is closed via the local closure current system and the remaining 32 percent via the Cowling closure current system. Sheng et al. (2014) deduced, based on the Constellation Observing System for Meteorology, Ionosphere, and Climate

55 (COSMIC) satellites observations from 2008 to 2011, the height-integrated northward and westward conductivities in both E (100–150 km) and F (150–600 km) regions and their ratio. The maximum ratio in the northern summer hemisphere is 5.5, which is smaller than that from the Thermosphere-Ionosphere-Electrodynamics General Circulation Model (TIE-GCM v1.94) simulation which is 9. It was assumed that the energy inputs into the F region may be underestimated in the model. Tulegenov and Streltsov (2019) investigated the role of the Hall conductivity in ionospheric heating experiments. Ionospheric heating by

60 powerful X-mode waves changes the Hall and Pedersen conductances in the E and D regions, which lead to the generation of

ultra-low frequency (ULF)/ELF/very low frequency (VLF) waves, when the electric field exists in the ionosphere. Tanaka et al. (2020) identified shell currents in the ionosphere from ground based magnetic variations using Biot-Savar's law. Robinson et al. (2020) determined height-integrated conductances in the ionosphere from the electron densities measured by a radar. Carter et al. (2020) parameterized the height-integrated conductances in the ionosphere by interplanetary magnetic field.

65   In the following sections, we present an analytical description of the shell-current system in the ionosphere considered as a relatively thick layer. First, a smooth transition of the tangential-to-the-layer component of the magnetic field from zero below the ionosphere to non-zero tangential component above the ionosphere is provided in the layer. Then the current density is determined from it. After that, the Euler potentials are found for the ionosphere, which opens the way for precise determination of electrons and protons motion in the layer. The paper is organized in the following way. The Method is described in Section 2.
70 The results of the calculations of the magnetic field, current density, and the Euler potentials are outlined in Section 3, followed by Section 4 in which our conclusions are summarized.

2   Method

As our model ionosphere, we consider only a denser part of the real ionosphere, in heights 100–400 km. Euler potentials of the inner region, below the ionosphere, $r < r_{\rm in} = 1.0157\,r_0$ (height 100 km above Earth's surface), are

$$\alpha = \alpha_d = \frac{B_0\,r_0^3\sin^2\theta}{r},\ \beta_{\rm in} = \beta_d = -\varphi. \tag{1}$$

75 The variables are spherical coordinates r, θ, and φ, with the origin at Earth's center and the z axis coinciding with the magnetic axis and pointing to North. The φ angle is measured from an arbitrary equatorial point, because our problem is axially symmetric. Here, B_0 is determined by the Earth's magnetic dipole ($B_0 = 31.2\ \mu$T in the present paper), and r_0 is the Earth's radius (6378 km). The α_d and β_d are Euler potentials of a dipole. In the outer region, above the ionosphere ($r > r_{\rm out} = 1.0627\,r_0$, height 400 km), the Euler potentials are

$$\alpha = \alpha_d = \frac{B_0\,r_0^3\sin^2\theta}{r},\ \ \beta_{\rm out} = \beta_d + \beta_t = -\varphi + \frac{g_0\,r^2\cos\theta}{r_0^2\sin^4\theta}. \tag{2}$$

80 Here, g_0 is a unit-less quantity which determines the magnitude of FACs. Its evaluation is described in Romashets and Vandas (2020), where it is based on observations by Korth et al. (2010). The transition takes place in the layer of thickness $\Delta r = r_{\rm out} - r_{\rm in}$ (300 km). The r and θ components of the magnetic field are the same everywhere in our system. Only the φ component changes, from $B_{\varphi,\rm in} = 0$ in the inner region to

$$B_{\varphi,\rm out} = \frac{B_0\,g_0\,r_0}{r\sin\theta} \tag{3}$$

in the outer region. This component in the layer experiences a smooth change from its value below the ionosphere to one above
85 the ionosphere. In the entire volume, in the ionosphere, above and below the ionosphere, it is modeled by a step-up, $\tanh$, function:

$$B_\varphi = \frac{B_0 g_0 r_0}{2r\sin\theta}\left[1 + \tanh\frac{6(r - r_c)}{\Delta r}\right]. \tag{4}$$

Here, $r_c = (r_{\mathrm{in}} + r_{\mathrm{out}})/2$. The φ component above r_{out} and below r_{in} approaches the values provided correspondingly by Eq. (1) and Eq. (2) very rapidly. With Eq. (4), the observed magnetic field profiles are well described. The transition from the magnetic field determined by Eq. (1) to the magnetic field determined by Eq. (2) happens mostly inside the ionosphere. On the

90 other hand, at a much smaller rate, the transition continues outside of the ionosphere as well. And the currents producing the change are mostly confined inside the ionosphere. Such a usage of the step-up function is not new. It was utilized widely, for example, by Landau and Lifshitz (1981), in quantum mechanics applications for description of potential energy of electrons in metals.

The Euler potentials for a magnetic field in the ionosphere are searched, because the charged particles motion can be easily

95 calculated with them (Romashets and Vandas , 2011, 2012; Vandas and Romashets , 2014, 2016). In order to provide that the φ component of the magnetic field in the layer changes with r according to Eq. (4), we will keep α the same as in Eqs. (1) and (2), while β is determined from

$$B_\varphi = \frac{1}{r} \left(\frac{\partial \alpha}{\partial r} \frac{\partial \beta}{\partial \theta} - \frac{\partial \beta}{\partial r} \frac{\partial \alpha}{\partial \theta} \right). \tag{5}$$

This latter equation can be solved for β by various approximation methods. An important condition for β is that it should be continuous in the layer and around it, for proper determination of magnetic field lines and particle trajectories. One of the

100 methods decomposes Eq. (4) into the sum

$$B_\varphi = \frac{B_0 g_0 r_0}{r \sin \theta} \sum_{i=1}^{I} c_i \left(\frac{r}{r_0} \right)^{n_i}. \tag{6}$$

The coefficients c_i are determined from the best fit to the step-up function

$$\mathrm{st}(r) = \frac{1}{2} \left[1 + \tanh \frac{6(r - r_c)}{\Delta r} \right] \tag{7}$$

by the sum

$$\mathrm{sm}(r) = \sum_{i=1}^{I} c_i \left(\frac{r}{r_0} \right)^{n_i}. \tag{8}$$

There is a problem that it is not possible to decompose Eq. (7) into the sum of power functions in Eq. (8) on the entire interval $(r_{\mathrm{in}}, r_{\mathrm{out}})$, but it can be done on any fraction of the interval of the length which is one third of it or less. This follows

105 directly from the fact that the corresponding Taylor sum of the st function has a radius of convergence one sixth of the interval. Therefore, we used four smaller overlapping intervals (subintervals), covering the entire interval, and determined the coefficients c_i for them separately. Details are given in Appendix A. We used $n_1 = -1.8$, $n_i = -1.8 + 19.8(i-1)/30$ for $I \geq i > 1$, and $I = 30$ for all subintervals. The choice of n_i values for the selected I was determined from the best agreement between Eqs. (8) and (7), by trials and errors. We have found that the number I larger than 30 does not improve the agreement

110 between the two functions in our calculations (using double precision).

The β potential in Eq. (5) is searched in the form

$$\beta = -\varphi + \sum_{i=1}^{I} c_i R_i(r) \Theta_i(\theta). \tag{9}$$

Inserting this β into Eq. (5) and equating the terms with the same c_i between Eqs. (5) and (6), we can determine $R_i(r)$ and $\Theta_i(\theta)$. Taking into account that α in Eqs. (1)–(2) depends on r as $\frac{1}{r}$, we conclude that R_i should be

$$R_i = g_0 \left(\frac{r}{r_0} \right)^{n_i+2}. \tag{10}$$

115 On the other hand, Θ_i should satisfy

$$\frac{1}{\sin\theta} = -\sin^2\theta\,\Theta_i' - (2n_i+4)\sin\theta\cos\theta\,\Theta_i, \tag{11}$$

which can be integrated by a method of variable coefficients. The prime means a derivative. The solution is

$$\Theta_i = -\frac{\operatorname{sgn}(\cos\theta)}{2(1+n_i)\sin^2\theta}\,{}_2F_1\left(\frac{1}{2}, 1+n_i, 2+n_i; \sin^2\theta\right). \tag{12}$$

Here, the sgn is the signum function and ${}_2F_1$ is the hypergeometric function. The entire interval (r_{in}, r_{out}) is divided into four parts as described in Appendix A and β is found for each part of the interval. The β in the first part of the interval is

$$\beta_1 = -\varphi + \sum_{i=1}^{I} c_{1,i} R_{1,i} \Theta_{1,i}. \tag{13}$$

The coefficients $c_{2,i}$, $c_{3,i}$ and $c_{4,i}$ are determined for the remaining parts of the interval, which means that β is also determined
120 in these parts. The coefficients are different and β may initially experience jumps at the interfaces from one part to another one, and at the ends of the entire interval. The jumps are removed with proper calibration of β. Romashets and Vandas (2024) and Vandas and Romashets (2024) proposed a technique which allows us to avoid the discontinuities in β at interfaces. The β in the second, third, and fourth parts should be adjusted by addition of functions of α. Graphically, this can be explained as a plot of a difference of β versus α along the interface, see for details Vandas and Romashets (2024). Once this function $f_2 = f_2(\alpha)$
125 is determined, then continuous β, a rectified β in the second part, is

$$\beta = \beta_2 + f_2(\alpha). \tag{14}$$

Similarly, in the third part

$$\beta = \beta_3 + f_3(\alpha), \tag{15}$$

and analogically for the fourth part (see Appendix A for details).

Knowledge of B_φ in the transition layer, Eq. (4), allows explicit expressions of the current density components, and of the current density magnitude. Using the equation $\boldsymbol{J} = \frac{1}{\mu_0}\nabla \times \boldsymbol{B}$, where μ_0 is the vacuum magnetic permeability, the components
130 are

$$
\begin{aligned}
J_r &= 0, \\
J_\theta &= -\frac{3B_0\,g_0\,r_0}{\mu_0\Delta r\,r\sin\theta}\,\operatorname{sech}^2\left[\frac{6(r-r_c)}{\Delta r}\right], \\
J_\varphi &= 0.
\end{aligned}
\tag{16}
$$

The maximum current density is reached in the middle of the layer.

3 Results

The φ component of the magnetic field in the entire interval for $\theta = \pi/6$ is shown in Figure 1. We use $g_0 = 0.006$, which corresponds to significant geomagnetic activity levels (Romashets and Vandas , 2020, 2022). The electric-current-density θ

135 component from Eq. (16) is depicted in Figure 2. The fit of the step-up function in the ionosphere is shown in Figure 3.
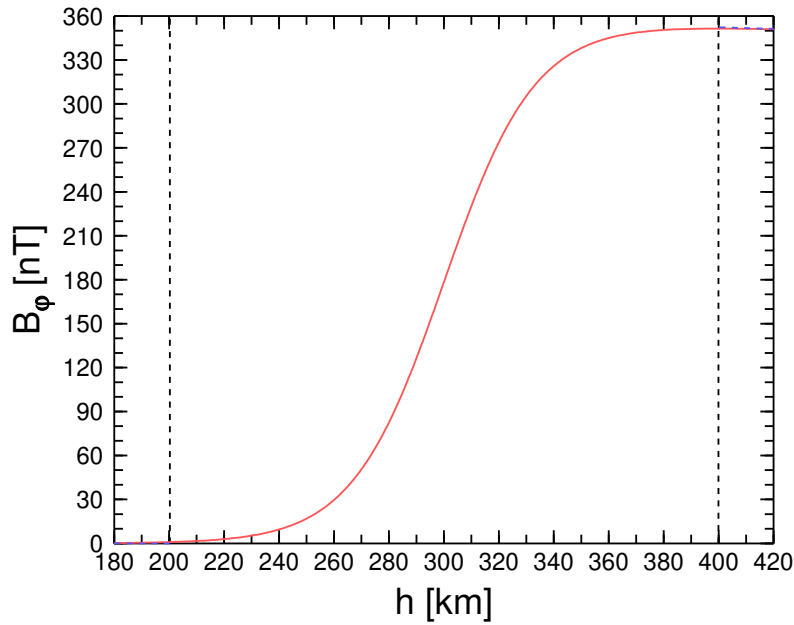
Figure 1. The φ component of the magnetic field in the ionosphere for $\theta = \pi/6$ from Eq. (4). The interval $(r_{\mathrm{in}}, r_{\mathrm{out}})$ is marked by dashed vertical lines.

Using the α from Eq. (1) and the rectified β, we calculated the magnetic field using

$$\boldsymbol{B} = \nabla\alpha \times \nabla\beta \tag{17}$$

and numerical differentiation. The original φ component of the magnetic field, Eq. (4), is compared to that calculated with Eq. (17) in Figure 4. The coincidence is excellent.

4 Discussion

140 The transition from one region to another one in Cartesian coordinates can demonstrate the approach better. Let us consider a planar layer $-x_0 < x < x_0$. The pair of Euler potentials in the layer

$$\alpha = B_0\left(y - \frac{x}{2} - \frac{x_0}{6}\log\cosh\frac{3x}{x_0}\right), \ \beta = z. \tag{18}$$
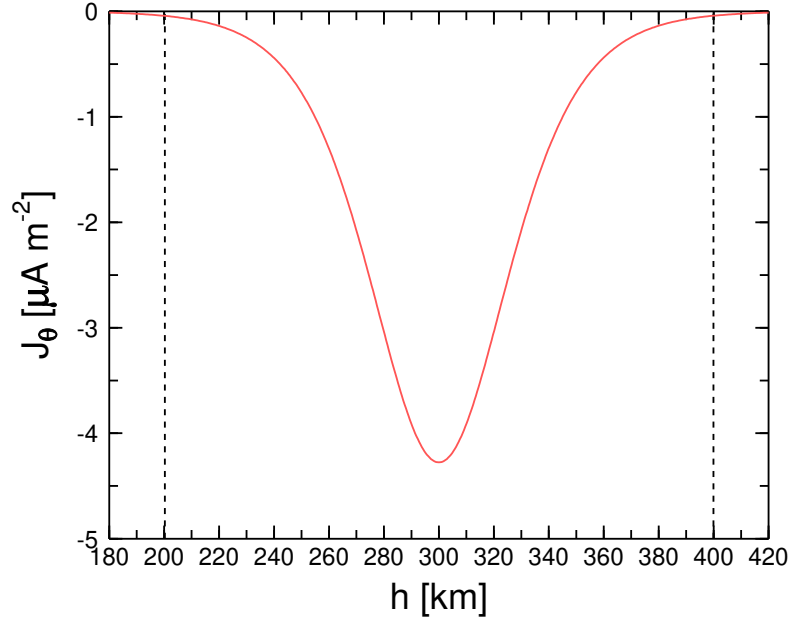
Figure 2. The θ component of the electric current density in the ionosphere for $\theta = \pi/6$ from Eq. (16). The interval $(r_{\text{in}}, r_{\text{out}})$ is marked by dashed vertical lines.

provide that the y-component of the magnetic field is smoothly changing:

$$B_y = \frac{1}{2} B_0 \left(1 + \tanh \frac{3x}{x_0} \right). \tag{19}$$

This magnetic-field component is plotted in Figure 5. There is a smooth change from $B_y \approx 0$ at $x = -x_0$ to $B_y \approx B_0$ at $x = x_0$. The dependence of α on x is demonstrated in Figure 6. The current density in the layer has only z-component,

$$J_z = \frac{3B_0}{2\mu_0} \frac{\text{sech}^2 \frac{3x}{x_0}}{x_0}. \tag{20}$$

145 Its maximum (J_{max}) is reached in the middle of the layer. The profile of the electric-current density z-component given by Eq. (20) is depicted in Figure 7. In Cartesian coordinates, one can easily deal with both tangential to the layer coordinates and provide a smooth transition from their values in one region to another.

Returning to our spherical system in the ionosphere, it is interesting to see that in addition to the toroidal component above the ionosphere, which is associated with the θ-component of the current density in the ionosphere, we can also consider the

150 transition of the poloidal (θ) component of the magnetic field. The magnetic field above the ionosphere is provided by the scalar potential, applicable for $\theta_1 > \theta > \theta_2$, where the magnetic field components are finite,

$$\Psi = B_0 r_0 g_0 \frac{\cos \varphi \sqrt{1 - \cos \theta}}{\sqrt{1 + \cos \theta}}, \tag{21}$$
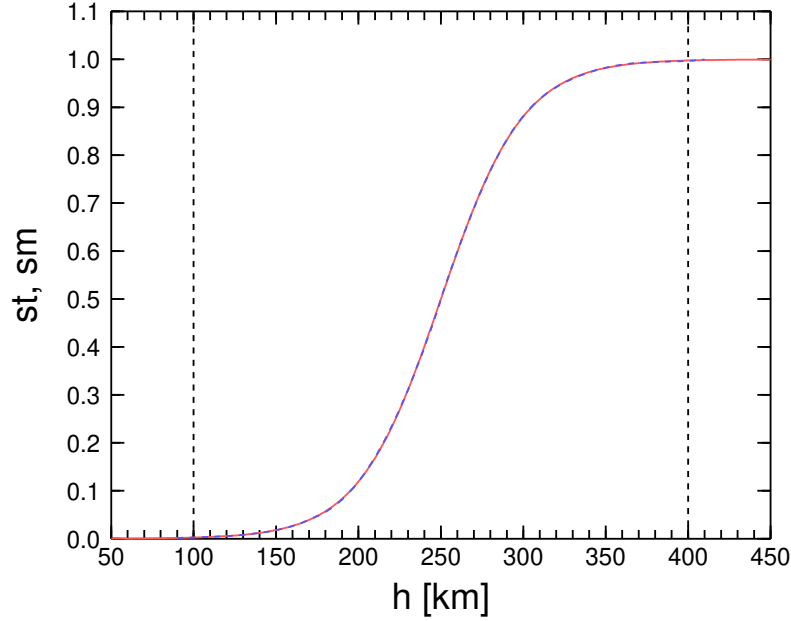
Figure 3. Fit of the step-up function, Eq. (7), red line, by a sum of power functions, Eq. (8), dashed blue line, in the ionosphere. The interval $(r_{\mathrm{in}}, r_{\mathrm{out}})$ is marked by dashed vertical lines.

is given by

$$B_r = 0, \tag{22}$$

$$B_\theta = \frac{B_0 r_0 g_0 \cos\varphi}{r(1+\cos\theta)}, \tag{23}$$

$$B_\varphi = -\frac{B_0 r_0 g_0 \sin\varphi \sqrt{1-\cos\theta}}{r\sin\theta\sqrt{1+\cos\theta}}. \tag{24}$$

It is current-free. The magnetic field in the ionosphere which corresponds to Eqs. (22)–(24) has components as given by Eqs. (22)–(24), but each multiplied by the function st from Eq. (7). In a similar fashion, described in Method, the Euler potentials and current density in the ionosphere are found. Combining Eq. (3) and Eqs. (22)–(24), we can model locally a real ratio between Pedersen and Hall currents. The radial component is absent in Eqs. (22)–(24), this is tangential discontinuity, due to special selection of the harmonic in Eq. (21), which does not depend on r.

5 Conclusions

It is important to construct the Euler potentials α and β for the study of charged-particles motion in the medium. It is especially convenient to have α and β expressed in a compact analytical form. In this work, we found continuous Euler potentials in the finite thickness contact discontinuity and applied them for the shell currents in the ionosphere. The result opens the way for studies of fine structure of such kind of discontinuities in the solar wind, magnetosphere, and interstellar space. The procedure
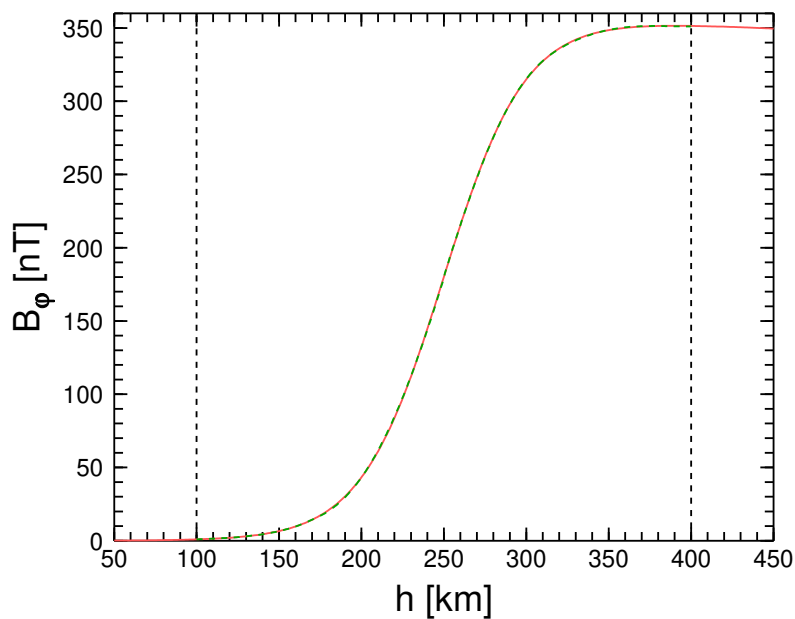
Figure 4. The given (red line) and model (dashed green line) φ component of the magnetic field in the ionosphere. The model B_φ was calculated from α and β by numerical differentiation. The interval $(r_{\mathrm{in}}, r_{\mathrm{out}})$ is marked by dashed vertical lines.
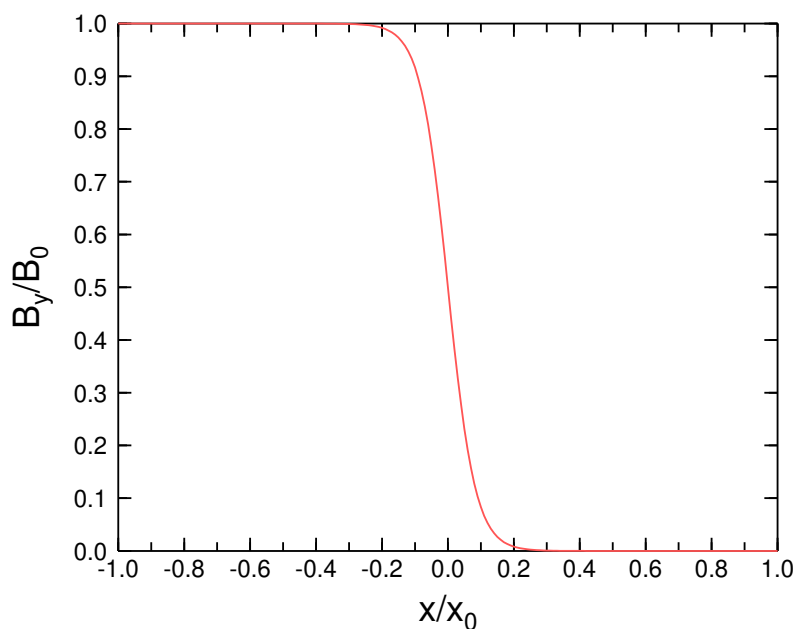
Figure 5. B_y in the layer.
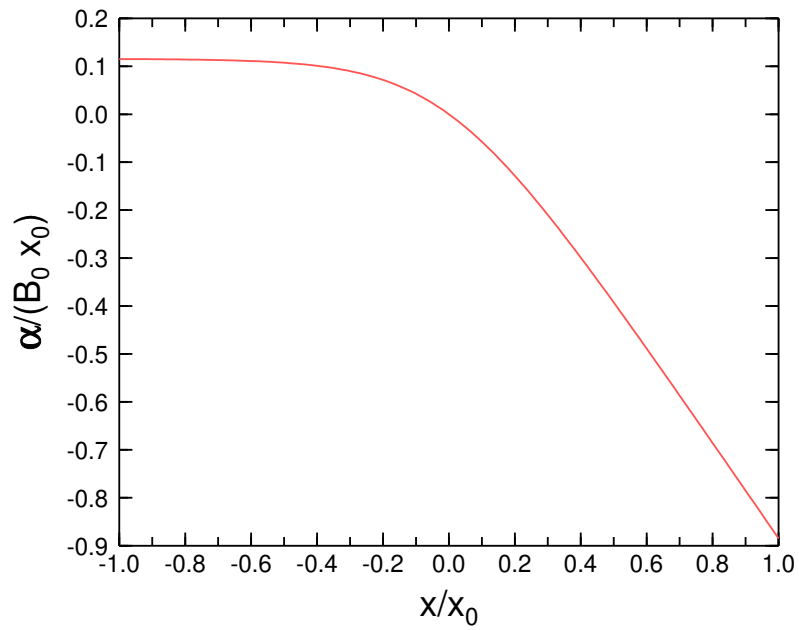
Figure 6. Euler potential α in the layer for $y = 0$.
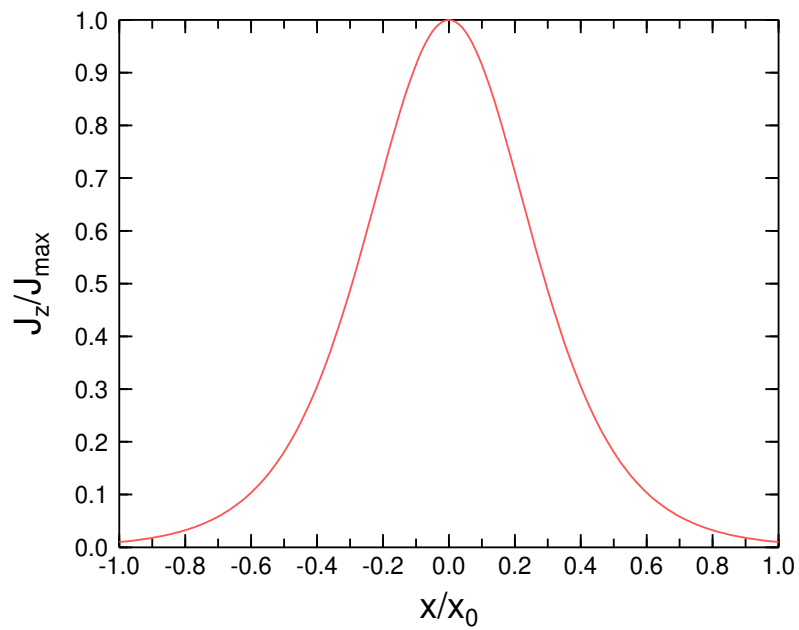
Figure 7. Current density in the layer.

consists of three steps. First, the magnetic field in the interface region is obtained, which represents a smooth transition from the magnetic field on one side to another one. Second, the region is divided into four parts and the Euler potentials are derived for each of them. One of the potentials, α, is the same, but there are four betas, one for each part of the interval. Next, because

170 the addition to β of a function of α does not change the resulting magnetic field, we add needed functions to betas in each part of the interval, and provide continuity of β in the interface region (the ionosphere in our case) and on its boundaries.

Appendix A: Determination of the coefficients c_i and rectification of β

We divide the interval $\langle r_{\mathrm{in}}, r_{\mathrm{out}} \rangle$ into four subintervals of equal lengths, $\langle r_{\mathrm{in}}, r_{12} \rangle$, $\langle r_{12}, r_{23} \rangle$, $\langle r_{23}, r_{34} \rangle$, and $\langle r_{34}, r_{\mathrm{out}} \rangle$ where $r_{12} = r_{\mathrm{in}} + (r_{\mathrm{out}} - r_{\mathrm{in}})/4$, $r_{23} = r_{\mathrm{in}} + 2(r_{\mathrm{out}} - r_{\mathrm{in}})/4$, and $r_{34} = r_{\mathrm{in}} + 3(r_{\mathrm{out}} - r_{\mathrm{in}})/4$. For each subinterval, we determine the

175 coefficients separately. Let us consider the first subinterval. We require

$$
\int_{\frac{1}{2}(r_{\mathrm{in}}+r_{12})-\frac{1}{6}\Delta r}^{\frac{1}{2}(r_{\mathrm{in}}+r_{12})+\frac{1}{6}\Delta r} [\mathrm{sm}(r) - \mathrm{st}(r)]^2 \, \mathrm{d}r
$$

$$
= \int_{\frac{1}{2}(r_{\mathrm{in}}+r_{12})-\frac{1}{6}\Delta r}^{\frac{1}{2}(r_{\mathrm{in}}+r_{12})+\frac{1}{6}\Delta r} \left[\sum_{i=1}^{I} c_{1,i} \left(\frac{r}{r_0} \right)^{n_i} - \mathrm{st}(r) \right]^2 \, \mathrm{d}r = \min \tag{A1}
$$

where the integration is over an interval of the length $\Delta r/3$ symmetrically overlapping the subinterval in play. Following the standard procedure for minimization, we differentiate Eq. (A1) by $c_{1,k}$ and set it to zero, finally obtaining

$$
180 \quad \sum_{i=1}^{I} c_{1,i} \int_{\frac{1}{2}(r_{\mathrm{in}}+r_{12})-\frac{1}{6}\Delta r}^{\frac{1}{2}(r_{\mathrm{in}}+r_{12})+\frac{1}{6}\Delta r} \left(\frac{r}{r_0} \right)^{n_i+n_k} \mathrm{d}r = \int_{\frac{1}{2}(r_{\mathrm{in}}+r_{12})-\frac{1}{6}\Delta r}^{\frac{1}{2}(r_{\mathrm{in}}+r_{12})+\frac{1}{6}\Delta r} \mathrm{st}(r) \left(\frac{r}{r_0} \right)^{n_k} \mathrm{d}r \tag{A2}
$$

which for $k = 1, \ldots, I$ represents a set of linear equations for $c_{1,i}$ that is solved. The integrals on the left-hand side of Eq. (A2) can be done analytically. We proceed in the same way for the remaining subintervals 2–4 and thus obtain four sets of the c_i coefficients, which determine four functions, β_1, β_2, β_3, and β_4, by Eq. (13). These functions are independent and one cannot expect that neighboring betas will have the same values at the interface (e.g., β_1 and β_2 at r_{12}); Figure A1(a) demonstrates this.

185 To make β continuous in the whole interval $\langle r_{\mathrm{in}}, r_{\mathrm{out}} \rangle$, we follow a procedure of rectification described in Vandas and Romashets (2024). It relies on the fact, that when a function of α is added to β, it has no effect on the related magnetic field. We define $\beta = \beta_1$ for $r < r_{12}$. The β_2 is adjusted in the following way. The α at the interface r_{12}, $\alpha = B_0 r_0^3 \sin^2\theta / r_{12}$, is a function of θ only. We introduce its inverse function

$$
\theta_{12}(\alpha) = \arcsin \sqrt{\frac{\alpha \, r_{12}}{B_0 \, r_0^3}}. \tag{A3}
$$

190 The adjusted β_2, denoted β_{2a}, is

$$
\beta_{2a}(r, \theta, \varphi) = \beta_2(r, \theta, \varphi) + \beta_1\{r_{12}, \theta_{12}[\alpha(r,\theta)], 0\} - \beta_2\{r_{12}, \theta_{12}[\alpha(r,\theta)], 0\}. \tag{A4}
$$

We define $\beta = \beta_{2a}$ for $r \in \langle r_{12}, r_{23} \rangle$. Similarly, the adjusted β_3 is

$$\beta_{3a}(r,\theta,\varphi) = \beta_3(r,\theta,\varphi) + \beta_{2a}\{r_{23},\theta_{23}[\alpha(r,\theta)],0\} - \beta_3\{r_{23},\theta_{23}[\alpha(r,\theta)],0\}, \tag{A5}$$

and analogically β_{4a}. We define $\beta = \beta_{3a}$ for $r \in \langle r_{23}, r_{34} \rangle$ and $\beta = \beta_{4a}$ for $r > r_{34}$. This rectified β is shown in Figure A1(b).
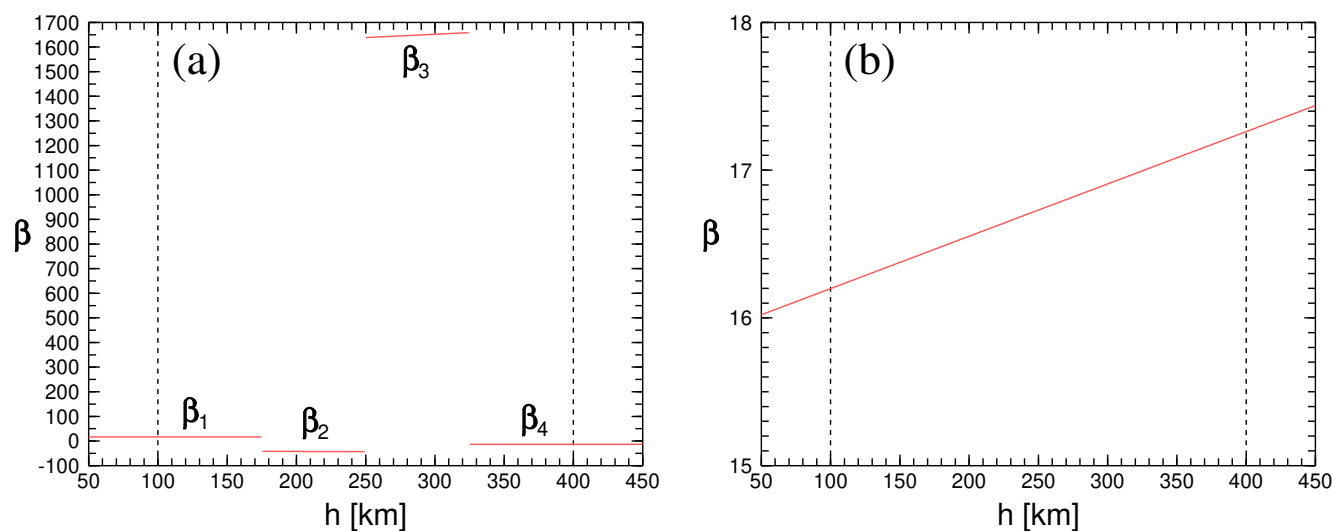
Figure A1. The Euler potential β (a) before and (b) after additions of functions $f(\alpha)$.

195 *Author contributions.* E.R. suggested the method for alpha and beta determination, M.V. suggested the way of beta correction, and made calculations and figures, both authors wrote the text and made editing.

Competing interests. No competing interests are present.

Acknowledgements. We would like to thank numerous colleagues for discussions. Stefaan Poedts provided especially useful comments. This research was supported by the NSF grant 2230363. M. V. acknowledges support from the AV ČR grant RVO:67985815 and the GA ČR grant 200 21-26463S.

References

Amm, O.: The elementary current method for calculating ionospheric current systems from multisatellite and ground magnetometer data, *J. Geophys, Res.*, **106**, 24843, doi:10.1029/2001JA900021, 2001.

Amm, O. and Fujii, R.: Separation of Cowling channel and local closure currents in the vicinity of a substorm breakup spiral, *J. Geophys. Res.*, **113**, A06304, doi:10.1029/2008JA013021, 2008.

Araki, T., Schlegel, K., and Luehr, H.: Geomagnetic effects of the Hall and Pedersen current flowing in the auroral ionosphere, *J. Geoph. Res.*, **94**, 17185, doi:10.1029/JA094iA12p17185, 1989.

Banks, P.M. and Yasuhara, F.: Electric fields and conductivity in the night time E-region: A new magnetosphere-ionosphere-atmosphere coupling effect, *Geophys. Res. Lett.*, **5**, 1047, doi:10.1029/GL005i012p01047, 1978.

Baumjohann, W.: Ionospheric and field-aligned current systems in the auroral zone: a concise review, *Adv Space Res.*, **2**, 55, doi:10.1016/0273-1177(82)90363-5, 1982.

Carter, J.A., Milan, S.E., Paxton, L.J., Anderson, B.J., and Gjerloev, J.: Height-integrated ionospheric conductances parameterized by interplanetary magnetic field and substorm phase, *J. Geophys. Res.*, **125**, e28121, doi:10.1029/2020JA028121, 2020.

Devasia, C.V. and Reddy, C.A.: Retrieval of east-west wind in the equatorial electrojet from the local wind-generated electric field, *J. Atm. Terr. Phys.*, **57**, 1233, doi:10.1016/0021-9169(94)00113-3, 1995.

Galand, M. and Richmond, A.D.: Ionospheric electrical conductances produced by auroral proton precipitation, *J. Geophys. Res.*, **106**, 117, doi:10.1029/1999JA002001, 2001.

Hosokawa, K., Ogawa, Y., Kadokura, A., Miyaoka, H., and Sato, N.: Modu311 lation of ionospheric conductance and electric field associated with pulsating aurora, *J. Geophys. Res.*, **115**, A03201, doi:10.1029/2009JA014683, 2010.

Kamide, Y.R. and Brekke, A.: Altitude of the eastward and westward auroral electrojets, *J. Geophys. Res.*, **82**, 2851, doi:10.1029/JA082i019p02851, 1977.

Kintner, P.M., Cahill, L.J., and Arnoldy, R.L.: Current system in an auroral substorm, *Journal of Geophysical Research*, **79**, 4326, doi:10.1029/JA079i028p04326, 1974.

Kirkwood, S., Opgenoorth, H., and Murphree, J.S.: Ionospheric conductivities, electric fields and currents associated with auroral substorms measured by the EISCAT radar, *Planet. Space Sci.*, **36**, 1359, doi:10.1016/0032-0633(88)90005-0, 1988.

Korth, H., Anderson, B.J., and Waters, C.L.: Statistical analysis of the dependence of large-scale Birkeland currents on solar wind parameters, *Ann. Geophys.*, **28**, 515, doi:10.5194/angeo-28-515-2010, 2010.

Landau, L. D., Lifshitz, L. M.: Quantum Mechanics: Non-Relativistic Theory, Course of Theoretical Physics, Volume 3, Third Edition. Butterworth- Heinemann, 1981.

Opgenoorth, H.J., Pellinen, R.J., Baumjohann, W., Nielsen, E., Marklund, G., and Eliasson, L.: Three-dimensional current flow and particle precipitation in a westward travelling surge (observed during the barium-GEOS rocket ex331 periment), *J. Geophys Res.*, **88**, 3138, doi:10.1029/JA088iA04p03138, 1983.

Raghavarao, R., Sridharan, R., and Suhasini, R.: The importance of vertical 333 ion currents on the nighttime ionization in the equatorial electrojet, *J. Geophys. Res.*, **89**, 11033, doi:10.1029/JA089iA12p11033, 1984.

Robinson, R.M., Kaeppler, S.R., Zanetti, L., Anderson, B., Vines, S.K., Korth, H., and Fitzmaurice, A.: Statistical relations between auroral electrical conductances and field-aligned currents at high latitudes, *J. Geophys. Res.*, **125**, e28008, doi:10.1029/2020JA028008, 2020.

Romashets, E. and Vandas, M.: Euler potentials for the Earth magnetic field with field-aligned currents, *J. Geophys. Res.*, **125**, e28153, doi:10.1029/2020JA028153, 2020.

Romashets, E. and Vandas, M.: Exact Alpha-Beta Mapping of IGRF Magnetic Field in the Ionosphere, *J. Geophys. Res.*, **129**, e2023JA032131, doi:10.1029/2023JA032131, 2024.

Romashets, E.P. and Vandas, M.: Euler potentials for two line currents aligned with an ambient uniform magnetic field, *J. of Geophys. Res.*, **116**, A09227, doi:10.1029/2011JA016595, 2011.

Romashets, E.P. and Vandas, M.: Euler potentials for two current sheets along ambient uniform magnetic field, *J. Geophys. Res.*, **117**, A07221, doi:10.1029/2012JA017587, 2012.

Romashets, E. and Vandas, M.: Euler potentials for Dungey magnetosphere with axisymmetric ring and field-aligned currents, *J. Geophys. Res.*, **127**, e30171, doi:10.1029/2021JA030171, 2022.

Rostoker, G. and Hron, M.: The eastward electrojet in the dawn sector, *Planet. Space Sci.*, **23**, 1377, doi:10.1016/0032-0633(75)90033-1, 1975.

Senior, C., Robinson, R.M., and Potemra, T.A.: Relationship between field-aligned currents, diffuse auroral precipitation and the westward electrojet in the early morning sector, *J. Geophys. Res.*, **87**, 10469, doi:10.1029/JA087iA12p10469, 1982.

Sheng, C., Deng, Y., Yue, X., and Huang, Y.: Height-integrated Pedersen conductivity in both E and F regions from COSMIC observations, *J. Atm. and Sol.-Terr. Phys.*, **115**, 79, doi:10.1016/j.jastp.2013.12.013, 2014.

Tanaka, T., Ebihara, Y., Watanabe, M., Den, M., Fujita, S., Kikuchi, T., Hashimoto, K. K., and Kataoka, R.: Reproduction of ground magnetic variations during the SC and the substorm from the global simulation and Biot-Savart's law, *J. Geophys. Res.*, **125**, e27172, doi:10.1029/2019JA027172, 2020.

Troshichev, O.A., Gizler, V.A., Ivanova, I.A., and Merkureva, A.I.: Role of field-aligned currents in generation of high-latitude magnetic disturbances, *Planet. Space Sci.*, **27**, 1451, doi:10.1016/0032-0633(79)90091-6, 1979.

Tulegenov, B. and Streltsov, A.V.: Effects of the Hall conductivity in ionospheric heating experiments, *Geophys. Res. Lett.*, **46**, 6188, doi:10.1029/2019GL083340, 2019.

Vandas, M. and Romashets, E.P.: Euler potentials for two layers with nonconstant current densities in the ambient magnetic field aligned to the layers, *Ann. Geophys.*, **34**, 1165, doi:10.5194/angeo-34-1165-2016, 2016.

Vandas, M.I. and Romashets, E.P.: Euler potentials for two current sheets of nonzero thickness along ambient uniform magnetic field, *J. Geophys. Res.*, **119**, 2579, doi:10.1002/2013JA019604, 2016.

Vandas, M. and Romashets, E.: Flux calibration of coronal magnetic field, *Solar Phys.*, **299**, 119, doi:10.1007/s11207-024-02364-1, 2024.

Werner, D.H. and Ferraro, A.J.: Mapping of the polar electrojet current down to ionospheric d region altitudes, *Radio Sci.*, **25**, 1375, doi:10.1029/RS025i006p01375, 1990.